CrossMark

Comparative evaluation of image quality among different detector configurations using area detector computed tomography

Yohei Miura[1,2] · Katsuhiro Ichikawa[3] · Ichiro Fujimura[2,4] · Takanori Hara[5] · Takashi Hoshino[6] · Shinji Niwa[2,5] · Masao Funahashi[1]

Abstract

The 320-detector row computed tomography (CT) system, i.e., the area detector CT (ADCT), can perform helical scanning with detector configurations of 4-, 16-, 32-, 64-, 80-, 100-, and 160-detector rows for routine CT examinations. This phantom study aimed to compare the quality of images obtained using helical scan mode with different detector configurations. The image quality was measured using modulation transfer function (MTF) and noise power spectrum (NPS). The system performance function (SP), based on the pre-whitening theorem, was calculated as MTF^2/NPS, and compared between configurations. Five detector configurations, i.e., 0.5×16 mm (16 row), 0.5×64 mm (64 row), 0.5×80 mm (80 row), 0.5×100 mm (100 row), and 0.5×160 mm (160 row), were compared using a constant volume CT dose index ($CTDI_{vol}$) of 25 mGy, simulating the scan of an adult abdomen, and with a constant effective mAs value. The MTF was measured using the wire method, and the NPS was measured from images of a 20-cm diameter phantom with uniform content. The SP of 80-row configuration was the best, for the constant $CTDI_{vol}$, followed by the 64-, 160-, 16-, and 100-row configurations. The decrease in the rate of the 100- and 160-row configurations from the 80-row configuration was approximately 30%. For the constant effective mAs, the SPs of the 100-row and 160-row configurations were significantly lower, compared with the other three detector configurations. The 80- and 64-row configurations were adequate in cases that required dose efficiency rather than scan speed.

Keywords Computed tomography · Helical scan · System performance function · Volume CT dose index · Detector configurations · Image quality

✉ Katsuhiro Ichikawa
ichikawa@mhs.mp.kanazawa-u.ac.jp

1 Department of Medical Technology, Osaka General Medical Center, Osaka, Japan

2 Graduate School of Medical Science, Kanazawa University, Kanazawa, Japan

3 Institute of Medical, Pharmaceutical and Health Sciences, Kanazawa University, 5-11-80 Kodatsuno, Kanazawa, Ishikawa 920-0942, Japan

4 Department of Radiological Technology, Rinku General Medical Center, Izumisano, Japan

5 Department of Medical Technology, Nakatsugawa Municipal General Hospital, Nakatsugawa, Japan

6 Department of Radiology, Ishinkai Yao General Hospital, Yao, Japan

1 Introduction

Multi-detector-row computed tomography (MDCT) provides high-quality CT images with high-speed scanning. Its effectiveness has been demonstrated in clinical studies [1–5]. The maximum coverage of MDCT in the z-direction is 160 mm with a 320- or 256-detector row CT. The 320-detector row CT system is effective for various diagnostic imaging owing to a wide coverage with fixed-table scanning, particularly for cardiac CT [6, 7]. The 320-detector row CT is also designed to enable helical scanning with detector configurations using 4-, 16-, 32-, 64-, 80-, 100-, and 160-detector rows for routine CT examinations. When the same pitch factor is used, the scanning speed of the MDCT increases with the detector row number (beam width). However, the effect of detector configuration on image quality is currently unknown;

although helical scanning is routinely used in CT examination, even with a 320-detector row CT, the operator can easily select one of the detector configurations while planning the scan. To our knowledge, a comparison of image quality while using different detector configurations has not been previously reported.

This phantom study aimed to compare the quality of images acquired during helical scans, with different detector configurations using a 320-detector row CT (area detector CT, ADCT). The images were evaluated using a system performance (SP) function estimated from measured modulation transfer function (MTF) and noise power spectrum (NPS).

2 Materials and methods

2.1 Detector configurations and scan conditions

We used an ADCT system (Aquilion One ViSION Edition; Toshiba Medical, Otawara, Japan) that had the geometries of a focus-isocenter distance of 600 mm, a focus-detector distance of 1072 mm, and a maximum cone angle of 7.59°. Five detector configurations, i.e., 0.5×16 mm (16 row), 0.5×64 mm (64 row), 0.5×80 mm (80 row), 0.5×100 mm (100 row), and 0.5×160 mm (160 row), were compared. The scan field of view was set to 320 mm, and the pitch factors for helical scans with a 16-, 64-, 80-, 100-, and 160-row configurations were set to 0.938, 0.828, 0.813, 0.810, and 0.806, respectively, assuming an abdominal CT examination for adults. All images were reconstructed with a 200-mm display field of view and a FC13 reconstruction kernel, using a reconstruction algorithm for routine helical scan, TCOT which uses a modified Feldkamp algorithm [8]. The nominal slice thicknesses were 1.0 and 5.0 mm. Considering the dose guidance level for an adult abdomen published by the International Atomic Energy Agency, the volume CT dose index ($CTDI_{vol}$) for the noise measurement was set at 25 mGy [9]. While actually setting the scan parameter, we took the phantom size into account, based on the size-specific dose estimate (SSDE) reported by American Association of Physicists in Medicine (AAPM) Task Group 204 [10]. The phantom used for noise evaluation was the uniformity module, CTP 486, in Catphan 600 (Phantom Laboratory, Salem, NY, USA), which has an outside diameter of 20 cm and a water-equivalent density. Thus, the actual absorbed dose is significantly increased and the noise is greatly reduced (underestimated) when the scan parameters for the $CTDI_{vol}$ of 25 mGy are used. To correct this, we used a conversion factor of 1.78 for the 20-cm diameter which was indicated in the SSDE report, and set the target $CTDI_{vol}$ to 14 ($\approx 25/1.78$) mGy.

According to the CTDI measuring method stated in the International Electrotechnical Commission (IEC) 60601-2-44 [11], we measured $CTDI_{vol}$s for the five detector configurations at a constant tube current—rotation time product of 100 mAs and 120 kV. From the measured values, the $CTDI_{vol}$ values per unit of mAs required to obtain the target $CTDI_{vol}$ were determined. An acrylic cylindrical CTDI phantom with a diameter of 32 cm and a Radcal electrometer model 9010 (Radcal Corp., Monrovia, CA) combined with a Radcal ionizing chamber model 10X5-3CT (Radcal Corp.) were used.

The beam width in the z-direction is generally wider than the full width of the detector, to prevent X-ray non-uniformity caused by focal spot penumbra. The wider beam, i.e., overbeaming, is the excess dose that is not used during CT scanning. The CTDI is based on the radiation dose profile in the acrylic cylindrical phantom, and thus, the beam width strongly affects the CTDI value. The greater the overbeaming, the greater the additional dose involved in the CTDI measurement. Therefore, when a constant CTDI is set for different detector widths with the same pitch factor, mAs values were more affected by the degree of overbeaming. Conversely, the effective mAs, which is calculated by dividing mAs by the helical pitch factor, is used to select the exposure dose level with approximately the same image noise at different pitch factors. Therefore, we performed another comparison with a constant effective mAs to examine how image quality was affected by the detector configuration, under conditions expected to have the same image noise. The constant effective mAs used in the current study was 185 mAs, based on the mAs value corresponding to the constant $CTDI_{vol}$ of 14 mGy using an 80-row detector.

2.2 Slice sensitivity profile and contrast measurements

To perform fair in-plane image quality comparisons between different detector configurations, it was important to confirm that the slice sensitivity profiles (SSPs) and object contrasts of the detector configurations tested were identical. Therefore, they were preliminarily measured using phantoms corresponding to the respective measurements. SSPs were measured using phantoms with point sources [12, 13]. A phantom with a 0.05-mm thickness and 1-mm diameter Tungsten microcoin, which is included in a quality control phantom set (MHT; Kyoto Kagaku Co., Kyoto, Japan), for 1.0-mm slice image and a phantom with a small lead bead with a 0.5-mm diameter (unknown model name; Kagaku Co., Kyoto, Japan) for 5-mm slice images were used. Each phantom was selected to obtain a sufficiently high accuracy of SSP measurement with both, high

CT values and correct responses, for each slice thickness. The scan conditions for all detector configurations were the same as those for the constant effective mAs because the SSP is not affected by radiation dose. The CT images were reconstructed with intervals of 0.1 mm, for the 1.0- and 5.0-mm slice thicknesses [12] to precisely detect the response of the microcoin and bead. The average values of the region of interest (ROI) placed at the point source were recorded and plotted with respect to the table position of each image after normalization, using the peak ROI value. The resultant SSP was obtained by averaging five SSP measurements. Figures 1 and 2 show the SSPs for 1.0- and 5.0-mm slice thicknesses. Full width at half maximum (FWHM) values of the 1-mm slice for the 16-, 64-, 80-, 100-, and 160-row configuration were 1.09, 1.06, 1.07, 1.06, and 1.03 mm, respectively. The full width at tenth maximum (FWTM) values were 1.86, 1.83, 1.84, 1.82, and 1.82 mm, respectively. The FWHM values of the 5-mm slice were 4.99, 5.00, 4.96, 4.96, and 4.95 mm, respectively, while the FWTM values were 5.77, 5.77, 5.80, 5.76, and 5.74 mm, respectively. The five SSPs had almost identical shapes for both 1.0- and 5.0-mm slice thicknesses, though some waviness was observed in the results of 5-mm slice thickness with 100- and 160-row configurations. Since the waviness was nearly identically reproduced in the five measurements, it was surmised that a sensitivity non-uniformity through the detector rows affected the SSP shapes.

The object contrast was measured using a low-contrast module, CTP515, in Catphan600, which was scanned using the same conditions as the constant effective mAs. Using CT images reconstructed with the 5-mm slice thickness, the CT value of a supra-slice target with 1.0% contrast
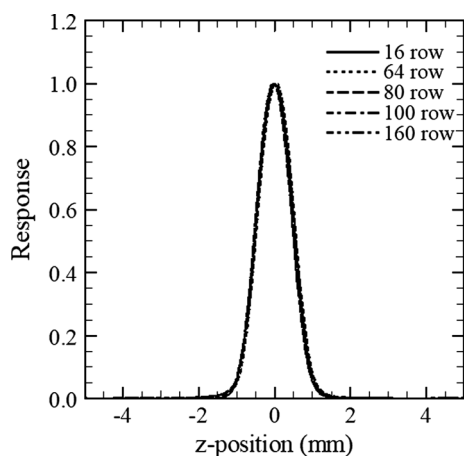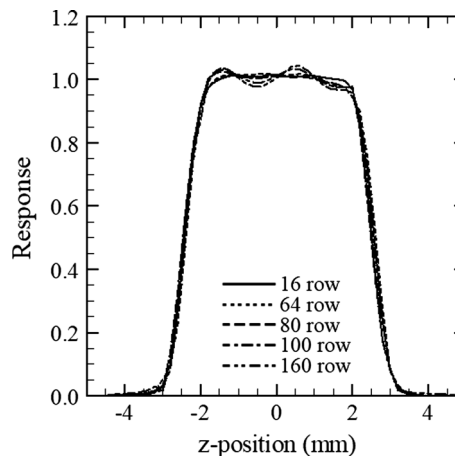

Fig. 2 Slice sensitivity profiles of a nominal slice thickness of 5.0-mm for the five detector configurations

(ΔHounsfield unit, ΔHU = 10) and a diameter of 15 mm was measured. The contrasts to background for the 16-, 64-, 80-, 100-, and 160-row configurations were also similar (i.e., 10.46, 10.27, 10.16, 10.26, and 10.25 HU, respectively). Therefore, we confirmed that fair image quality comparisons were possible using MTF and NPS as in-plane image quality indices.

2.3 MTF measurement

The MTF was measured using a wire phantom consisting of thin copper wires with a 0.16-mm diameter enclosed in a 50-mm-diameter cylindrical acrylic case filled with water [14, 15]. The scan conditions were same as those for the constant effective mAs because MTF is not affected by the radiation dose, similar to the SSP measurement. The phantom was aligned such that the wire was precisely perpendicular to the scan plane. The display field of view was set to 50 mm to obtain a correct impulse response with sufficient data points (i.e., a sufficiently small pixel pitch). A sub-image with 256×256 pixels centered on the wire was extracted from each wire CT image. Two-dimensional (2D) Fourier transform of the sub-image was then performed. The 2D result was then converted into a one-dimensional (1D) result using azimuthal averaging. Finally, the result was divided by the magnitude obtained at zero frequency to yield the MTF. We obtained 50 images with 1.0-mm slice thickness for each detector configuration and calculated the average MTF.

Fig. 1 Slice sensitivity profiles of a nominal slice thickness of 1.0-mm for the five detector configurations: 0.5×16 mm (16 row), 0.5×64 mm (64 row), 0.5×80 mm (80 row), 0.5×100 mm (100 row), and 0.5×160 mm (160 row)

2.4 NPS measurement

NPSs were measured from CT images using the uniformity module, CTP 486, in Catphan 600 scanned with 14 mGy (the constant $CTDI_{vol}$) and 185 mAs (the constant effective

mAs). We obtained 100 images for each detector configuration from a single scan for 1-mm slice thickness and five scans for 5-mm slice thickness, and then averaged the NPS values. For the NPS calculation, an established method using 2D Fourier transform was employed [16–18]. The ROI size was set to 128×128 pixels at the center of image. In addition, we measured the standard deviations (SD) as a simple noise index from images used for the NPS measurement for each detector configuration with the constant $CTDI_{vol}$. A region of interest (ROI) with 40×40 pixels was centrically placed on the image, and the average SD value was obtained from images for each detector configuration.

2.5 SP function

The contrast-to-noise ratio (CNR) has been used as an index of low-contrast detectability, which can be expressed as follows: $(ROI_M - ROI_B)/SD_B$, where ROI_M and ROI_B are CT values measured on a low-contrast object and background regions of interest, respectively, and the SD_B is the standard deviation of the background. However, the CNR is limited as it cannot be used to compare between images with different spatial resolution properties because the SD is simple pixel variance and does not evaluate the spatial frequency components in the noise. If the spatial resolution properties are different between the images obtained using different detector configurations, CNR is no longer a suitable index for comparing image qualities. Therefore, we measured SP as a function of spatial frequency, u, expressed as follows:

$$SP^2(u) = MTF^2(u)/NPS(u). \tag{1}$$

This function is included in the pre-whitening signal-to-noise ratio (SNR_{PW}) calculated using the following equation:

$$SNR_{PW}^2(u) = \int \frac{S^2(u) \times MTF^2(u)}{NPS(u)} du, \tag{2}$$

where $S(u)$ denotes a spectrum of signal to be detected [19]. This metric was also used to evaluate the detectability index of an iterative reconstruction CT image [20]. SNR_{PW} provides a figure of merit that incorporates the signal spectrum, $S(u)$, and SP, $MTF^2(u)/NPS(u)$, and can also be considered the weighted sum of $MTF^2(u)/NPS(u)$ with $S^2(u)$ [19]. Therefore, $SP(u)$ can be treated as an index of the inherent performance of the imaging system, based on the pre-whitening operation that cancels out the effect of the spatial resolution of each system [21]. Thus, by using SP, one can compare the performances of different systems as a function of spatial frequency, which relates to the detectability, without being affected by the spatial resolution difference.

3 Results

3.1 MTF

Figure 3 shows the MTF measurements using the five detector configurations. The frequencies of 50/10% MTF for the 16-, 64-, 80-, 100-, and 160-row configurations were 0.34/0.78, 0.33/0.78, 0.33/0.78, 0.33/0.78, and 0.32/0.78 cycles/mm, respectively. The 160-row configuration presented slightly lower values in the low-frequency region compared with the other detector configurations, which produced mostly identical MTFs.

3.2 SP function

Figures 4 and 5 show the $SP(u)$ results for the constant $CTDI_{vol}$ and effective mAs, respectively. When comparing the same $CTDI_{vol}$ and effective mAs, the $SP(u)$ curves of the five detector configurations were mostly parallel, while the relative relations between the five detector configurations were different. For the constant $CTDI_{vol}$ with both 1.0- and 5.0-mm slice thicknesses, the 80-row configuration was the best, followed by the 64-, 160-, 16-, and 100-row configurations. The decrease rates from the 80-row with 1.0-/5.0-mm slice thicknesses at 0.1 cycles/mm were 11/15, 22/33, 26/34, and 33/37%, and those at 0.5 cycles/mm were 10/12, 23/21, 28/29, and 34/33%, respectively. For the constant effective mAs with both 1.0- and 5.0-mm slice thicknesses, the five detector configurations were divided into two groups: one with the 16-, 64-, and 80-row configurations and the other with the 100- and 160-row configurations. The lower group with the 100- and 160-row configurations showed approximately 30% reduced SP compared with the higher group at both 0.1 and 0.5 cycles/mm.
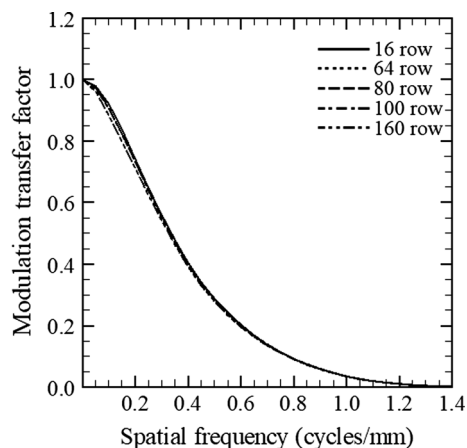

Fig. 3 Modulation transfer functions for the five detector configurations

Fig. 4 Graph showing the system performance function SP(u) with a constant $CTDI_{vol}$ of 14 mGy for **a** 1.0-mm slice thickness and **b** 5.0-mm slice thickness
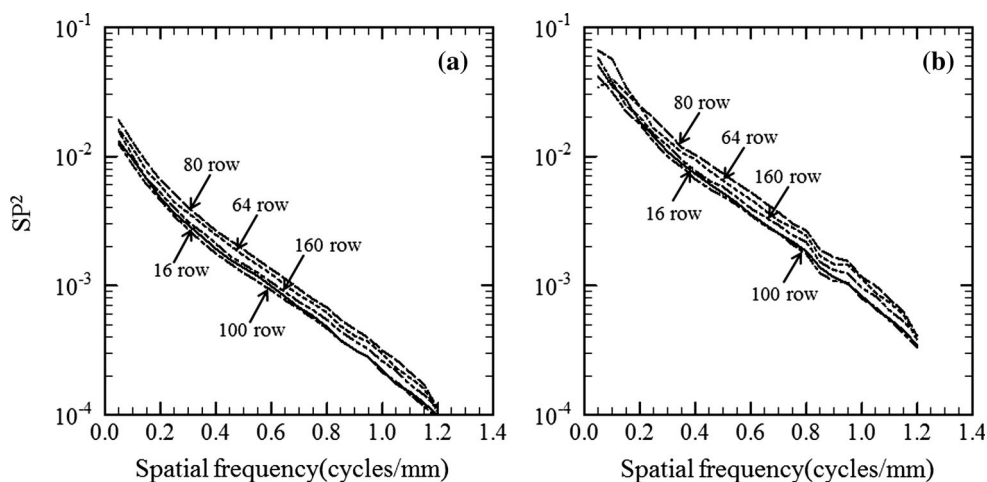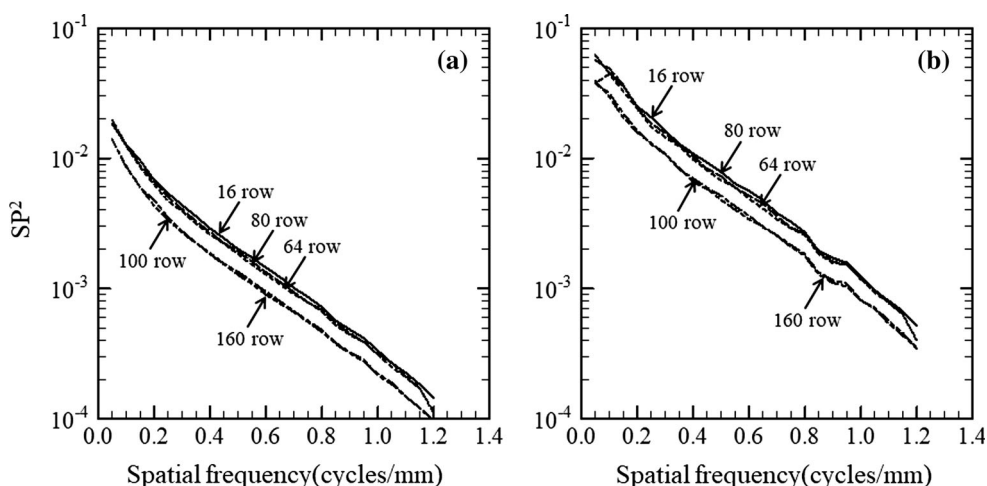

Fig. 5 Graph showing SP(u) with a constant effective mAs of 185 mAs for **a** 1.0-mm slice thickness and **b** 5.0-mm slice thickness

Since we confirmed sufficient reproducibility of the NPS measurement using 100 images and MTF measurement using 50 images in the preliminary investigation (SD less than 1% for NPS and 2% for MTF), we did not indicate the SD values or error bars in graphs in the SP results.

The SD values for the simple noise evaluation of 1-mm/5-mm slice thicknesses for the 16-, 64-, 80-, 100-, and 160-row configurations with the constant $CTDI_{vol}$ were 10.9/5.6, 9.5/4.9, 9.2/4.7, 11.1/5.7, and 10.1/5.2 HU, respectively.

4 Discussion

The maximum differences in the SP^2 between the five detector configurations were approximately 30% for both 1.0- and 5.0-mm slice thicknesses. These results should be considered during CT examinations, since the reported disagreement between nominal and measured $CTDI_{vol}$ values is < 5% [22].

Although we performed comparisons using the constant $CTDI_{vol}$ and effective mAs, the comparison using the constant $CTDI_{vol}$ was consistent with dose management in clinical CT examinations. It is known that SP^2 is proportional to the exposure dose to detector [19]. Thus, the relative SP^2 between the detector configurations can be treated like the relative sensitivity to radiation dose, and one can adjust the dose, referring to the SP^2 values.

Most of reconstruction kernels for adult abdominal CT have roll-off frequency properties, and the high spatial frequency components in the image are suppressed in such kernels [23]. Thus, it could be considered that SP values in the low frequency were important for the comparison. From our results, the MTF of the five detector configurations was almost the same, and the resultant SP^2 curves were almost parallel; thereby, a reasonably accurate comparison was possible between the detector configurations because the frequency balance was not changed by the change in detector configuration. Furthermore, this property was observed in both 1- and 5-mm slice thicknesses, and the order of SP was the same between the two slice

thicknesses. Therefore, our results indicated that the 80-row configuration was the best selection, while the 64-row configuration can be almost equally used, with an approximate 10% reduction in the SP compared to the 80-row configuration. However, the 100- and 160-row configurations with faster scan speeds might be required in some cases to prevent motion artifacts. In such cases, the 160-row configuration is more useful because of its better SP compared with the 100-row configuration. For obtaining image qualities equal to the 80-row configuration using the 100- and 160-row configurations, it can be estimated that an approximately 40% dose increase would be required.

In general, overbeaming was greater when using a narrower detector configuration [24] and the $SP(u)$ under a constant CTDI tended to become lower for such narrow detector configurations because greater overbeaming decreased the dose efficiency. However, according to our results, the 100- and 160-row configurations indicated approximately 35 and 30% reductions in SP compared with the 80-row, respectively, which was similar to the approximately 30% reduction in SP with the 16-row configuration.

This phenomenon can be understood by referring to the results of the comparison with the constant effective mAs. In this comparison, the 100- and 160-row configurations presented significantly lower SPs compared with the other three detector configurations. Under the constant effective mAs, nearly equal exposures for one helical rotation were given to all detector configurations. Thus, almost equal SPs were expected if the detector configuration (full beam width) does not affect SP. However, the 100- and 160-row configurations did not present equal SPs. Although we suspected that this could be attributed to the degradation of image quality caused by software scatter radiation corrections implemented for the 100- and 160-row configurations, it was very challenging to demonstrate this at a user level. However, it was considered that the SP degradations with the 100- and 160-row configurations shown in the results with the constant effective mAs appeared to relate to the low SPs of the two configurations for the constant $CTDI_{vol}$. For examining the reason of the degradations, SP comparisons using a non-helical scan might be effective. However, there is no established method (apparatus) to precisely measure SSP of the non-helical mode of CT with multi-detector rows. Therefore, since it was suspected that the SSPs were different between the detector configurations (especially between narrow and wide detector full widths) due to the Feldkamp algorithm, a fair SP comparison for non-helical scan was difficult without measuring the precise SSPs.

The full detector widths of recent 64-row MDCT systems can be classified into three widths, 32 (0.5×64), 38.4 (0.6×64), and 40.0 (0.625×64) mm, which are all used with 2D anti-scatter grids. In contrast, high-end MDCT systems with full detector widths of more than 40 mm (e.g., $0.625 \times 128 = 80$ mm, $0.6 \times 96 = 57.6$ mm, or $0.625 \times 256 = 160$ mm) are equipped with 3D anti-scatter grids, which have higher anti-scatter performances. Therefore, the elimination of more aggressive scatter radiation using the advanced anti-scatter grid might be effective for improving SPs from the 100- and 160-row configurations.

A few limitations of the current study must be noted. The methods used to measure the $CTDI_{vol}$ were not from the latest edition (Ed. 3.0: 2009) of the IEC60601-2-44 [9]. Thus, the 50-mm beam width $CTDI_{vol}$s for the 100-row configuration and 80-mm for the 160-row were underestimated by approximately 3 and 4%, respectively, according to the IEC60601 2-44 Ed. 3.1: 2012 [25]. The results of the 16-, 64-, and 80-row configurations were thought to be adequate because their beam widths were less than or equal to 40 mm, which did not require consideration regarding the wide beam problem. Given that the $CTDI_{vol}$s of the 100- and 160-row configurations were underestimated, the SP^2 values were overestimated by approximately 3 and 4%, respectively, because the NPS is known to be inversely proportional to radiation dose. Therefore, this did not affect our conclusion that the 100- and 160-row configurations caused the degradation of the SP under constant CTDI; this tendency would be emphasized by the $CTDI_{vol}$ measurement in the new edition of the IEC60601-2-44. We measured the NPS using the uniformity module in Catphan 600, which had a diameter of 200 mm. Though we corrected the $CTDI_{vol}$ using the conversion factor corresponding to the 20-cm diameter indicated in the SSDE report, beam hardening and scatter fraction remained uncorrected. Therefore, more practical comparisons using a water phantom with a 30-cm diameter should be conducted to evaluate the effect of detector configuration.

5 Conclusion

We compared the image qualities of five detector configurations for an ADCT helical scan using the SP function, $SP^2(u)$, calculated by $MTF^2(u)/NPS(u)$. Among the five detector configurations, the SP of 80-row configuration was the best, followed by the 64-, 160-, 16-, and 100-row configurations, respectively. Compared with the 80-row configuration, the 100- and 160-row configurations had decrease rates of approximately 30%. The results indicated that the 80- and 64-row configurations were adequate in cases where the dose efficiency was more important than the scan speed.

Compliance with ethical standards

References

1. Fleischmann D, Hallett RL, Rubin GD. CT angiography of peripheral arterial disease. J Vasc Interv Radiol. 2006;17:3–26.
2. Ahvenjärvi L, Niinimäki J, Halonen J, Tervonen O, Ojala R. Reliability of the evaluation of multidetector computed tomography images from the scanner's console in high-energy blunt-trauma patients. Acta Radiol. 2007;48:64–70.
3. Halpern EJ. Triple-rule-out CT angiography for evaluation of acute chest pain and possible acute coronary syndrome. Radiology. 2009;252:332–45.
4. Brandman S, Ko JP. Pulmonary nodule detection, characterization, and management with multidetector computed tomography. J Thorac Imaging. 2011;26:90–105.
5. Catalano O, De Bellis M, Sandomenico F, de Lutio di Castelguidone E, Delrio P, Petrillo A. Complications of biliary and gastrointestinal stents: MDCT of the cancer patient. Am J Roentgenol. 2012;199:187–96.
6. Fujimoto S, Matsutani H, Kondo T, Sano T, Kumamaru K, Takase S, Rybicki FJ. Image quality and radiation dose stratified by patient heart rate for coronary 64- and 320-MDCT angiography. Am J Roentgenol. 2013;200:765–70.
7. Khan A, Khosa F, Nasir K, Yassin A, Clouse ME. Comparison of radiation dose and image quality: 320-MDCT versus 64-MDCT coronary angiography. AJR Am J Roentgenol. 2011;197:163–8.
8. Angel E. AIDR 3D iterative reconstruction, a white paper by Toshiba America Medical Systems. 2012(2). http://www.medical.toshiba.com.
9. IAEA. IAEA safety standards series: radiological protection for medical exposure to ionizing radiation, No. RS-G-1.5. Vienna: International Atomic Energy Agency; 2002.
10. Boone JM, Strauss KJ, Cody DD, et al. Size-specific dose estimates (SSDE) in pediatric and adult body CT examinations. AAPM report No. 204. http://www.aapm.org; 2011.
11. IEC. Medical electrical equipment—Part 2-44: particular requirements for the basic safety and essential performance of
12. Hsieh J. Slice-sensitivity profile and noise. In: Computed tomography—principles, design, artifacts and recent advances. Bellingham, SPIE; 2003. pp. 150–3.
13. Ichikawa K, Kobayashi T, Sagawa M, Katagiri A, Uno Y, Nishioka R, Matsuyama J. A phantom study investigating the relationship between ground–glass opacity visibility and physical detectability index in low-dose chest computed tomography. J Appl Clin Med Phys. 2015;16:202–15.
14. Bischof CJ, Ehrhardt JC. Modulation transfer function of the EMI CT head scanner. Med Phys. 1977;4:163–7.
15. Boone JM. Determination of the presampled MTF in computed tomography. Med Phys. 2001;28:356–60.
16. Hanson KM. Detectability in computed tomographic images. Med Phys. 1979;6:441–51.
17. Kijewski MF, Judy PF. The noise power spectrum of CT images. Phys Med Biol. 1987;32:565–75.
18. Boedeker KL, Cooper VN, McNitt-Gray MF. Application of the noise power spectrum in modern diagnostic MDCT: part I. Measurement of noise power spectra and noise equivalent quanta. Phys Med Biol. 2007;52:4027–46.
19. International Commission on Radiation Units and Measurements. Medical imaging—the assessment of image quality. ICRU report No. 54. Bethesda: ICRU Publications; 1996.
20. Samei E, Richard S. Assessment of the dose reduction potential of a model-based iterative reconstruction algorithm using a task-based performance metrology. Med Phys. 2015;42:314–23.
21. Boedeker KL, McNitt-Gray MF. Application of the noise power spectrum in modern diagnostic MDCT: part II. Noise power spectra and signal to noise. Phys Med Biol. 2007;52:4047–61.
22. Trevisan D, Ravanelli D, Valentini A. Measurements of computed tomography dose index for clinical scans. Radiat Prot Dosim. 2014;158:389–98.
23. Takata T, Ichikawa K, Mitsui W, Hayashi H, Minehiro K, Sakuta K, Nunome H, Matsubara K, Kawashima H, Matsuura Y, Gabata T. Object shape dependency of in-plane resolution for iterative reconstruction of computed tomography. Phys Med. 2017;33:146–51.
24. Goo HW. CT radiation dose optimization and estimation: an update for radiologists. Korean J Radiol. 2012;13:1–11.
25. IEC. Medical electrical equipment—Part 2-44: particular requirements for the basic safety and essential performance of X-ray equipment for computed tomography. IEC publication No. 60601-2-44. Ed 3.1. Geneva: International Electrotechnical Commission; 2012.

X-ray equipment for computed tomography. IEC publication No. 60601-2-44. Ed 3.0. Geneva: International Electrotechnical Commission; 2009.